

Efficient Magic State Cultivation on the Surface Code

Yotam Vaknin,^{1,2} Shoham Jacoby,^{1,2} Arne Grimsmo,¹ and Alex Retzker^{1,2}

¹*AWS Center for Quantum Computing, Pasadena, CA 91125, USA*

²*Racah Institute of Physics, The Hebrew University of Jerusalem, Jerusalem 91904, Givat Ram, Israel*

(Dated: October 8, 2025)

Magic state cultivation is a newly proposed protocol that represents the state of the art in magic state generation. It uses the transversality of the H_{XY} gate on the 2D triangular color-code, together with a novel grafting mechanism to transform the color-code into a matchable code with minimal overhead. Still, the resulting code has a longer cycle time and some high weight stabilizers. Here, we introduce three new cultivation protocols, each yielding a different magic state. These protocols avoid grafting by exploiting transversal operations on the surface code using non-local connectivity, allowing for a much lower post-selection rates in the expansion process. Through numerical simulations, we demonstrate that our protocol achieves state-of-the-art infidelities and acceptance rates for magic state generation, on par with another recent proposal on the \mathbb{RP}^2 code, while still preserving the local geometry of the surface code. Moreover, in platforms such as cold atoms and trapped ions, where idle error rates are lower than two-qubit gate errors, we demonstrate that cultivation exhibits an even greater advantage, yielding an additional order-of-magnitude reduction in resource requirements. Lastly, we analyze the effect of erasure qubits on cultivation and show that *algorithmically-relevant* infidelities can be achieved using only 9 erasure qubits on a distance-2 surface code with a single cultivation round.

I. INTRODUCTION

Quantum error correction holds the promise of running quantum calculations with arbitrary precision on noisy physical qubits [1, 2]. As shown by Eastin and Knill [3], error correcting codes restrict the transversally accessible states within the code subspace to a finite set. To circumvent this limit, magic state injection [4, 5] and distillation [6, 7] were developed to generate specific states which enable fault-tolerant universal quantum computation.

Zero level distillation [8–14] reduces the distillation overhead by measuring an operator with non-stabilizer eigenstates on a single logical qubit. Repeated measurements project the qubit into a non-Clifford magic state with high fidelity. These protocols use a combination of post-selection and decoding to optimize the overhead and logical fidelity.

The recent magic state cultivation [15] protocol demonstrated a very low-overhead implementation of zero-level distillation. Cultivation grows an injected 2d triangular color-code [16–18] in stages, initially from $d = 3$ to $d = 5$ and later into a variation of the surface code [19–21], in a process called grafting.

The result of grafting is a combination of a color code and a surface code, that can be decoded using matching algorithms, such as Minimum Weight Perfect Matching [22]. Still, the grafted surface code has some weight 6 stabilizers, which doubles the CX depth of the syndrome extraction (SE) circuit.

Previous work mostly focused on codes with a transversal H gate, which can then be projectively measured. In this work, we describe, zero-level dis-

tillation directly on the surface code, which doesn't have a transversal H gate.

We begin by building on an idea first proposed by E. Dennis in 2001 [8] that first described $|CX\rangle$ state generation, and propose a new cultivation protocol based on the transversality of the CX gate. The protocol projects a pair surface codes into the two qubit $|CX\rangle$ magic state, which can be converted to a Toffoli magic state [8, 14].

We further expand our analysis to two *fold-transversal* gates [23]. We use the fold-transversality of the H and H_{XY} gate on the unrotated surface code, to measure it directly. Lastly, we measure the same *fold-transversal* gates mid-syndrome-cycle on the rotated surface code. This last protocol is economical in time and qubits, and results in the best overall rate.

The expansion step of the surface code is standard, followed by post-selection on the complementary gap similarly to Refs. [5, 15]. We show that our protocol utilizes the gap information better than color-code cultivation, resulting in similar fidelity and a significantly better rate.

Our magic state cultivation is designed using non-local transversal 3-qubit gates (CCX, CSWAP, CCZ) interaction between surface codes and a GHZ ancilla. Therefore, it would require either a native 3Q gate or compilation from 2Q interactions, and it is best suited for platforms with long range connectivity, such as Rydberg atoms [24]. In particular, utilizing the native CCZ gate available on Rydberg atom platforms, which has already been experimentally demonstrated in Refs. [25, 26].

We find that our scheme achieves an order-of-

magnitude improvement in success rate over color code cultivation at a target state fidelity of 10^{-7} , the level required in prior implementations of cryptographically relevant Shor's algorithms [27, 28]. This improvement mirrors the results of Chen et al. [29], which also exploit long-range connectivity to reach comparable infidelities, though within the \mathbb{RP}^2 geometry that relies on non-local boundaries. The key advantage of our approach over [29] is its inherent alignment with the surface-code geometry, allowing for straightforward implementation via transversal operations [23, 30].

Furthermore, most of those systems that support long range connectivity, and especially Rydberg-atom-based and ion-based computers, also exhibit much lower idling fidelity compared with two-qubit gates [30–34]. The noise model used in previous analysis assumed significant idling noise, under estimating the rate of cultivation in these systems. We find an additional order of magnitude improvement in rate when taking this effect into account, making magic state cultivation over $20\times$ faster than assumed in Rydberg atom resource estimation [27].

Lastly, we consider the effect of erasure and loss on magic state cultivation. Similar to [35], we show that the final logical fidelity is limited only by the non-identifiable noise, i.e. the residual Pauli rate. We describe a minimal protocol that can utilize significant erasure bias, and achieve below 10^{-6} fidelity using only 9 physical erasure qubits.

II. RESULTS

Zero level distillation is a set of protocols [8, 9, 11–13, 15, 36] that measure a logical operator directly on an error correcting code with a transversal gate. Different operators can be measured this way, each resulting in a different magic state. In [9, 11, 12] the Hadamard gate (H) is measured on a 2d triangular color-code, and we would follow this construction. Alternative gate choices are $H_{XY} = \frac{X+Y}{\sqrt{2}}$ measured in [15], and the 3 qubit operator $X \otimes CX$ is measured in [36].

A GHZ state, $|0\rangle^{\otimes n} + |1\rangle^{\otimes n}$ (normalization omitted), is generated with some correspondence between its qubits the qubits in the code, followed by a transversal control- H (CH) operation between a GHZ state and the data qubits of the code as the target. If H is a transversal operator on the code, then the GHZ state is affected by a phase kick-back. The state of the GHZ ancilla would be one of the two $|0\rangle^{\otimes n} \pm |1\rangle^{\otimes n}$ states, with the sign labeling the eigenvalue of H onto which the code was projected. Measuring the state of the GHZ ancilla effectively measures the logical H operator. Alternatively, the mea-

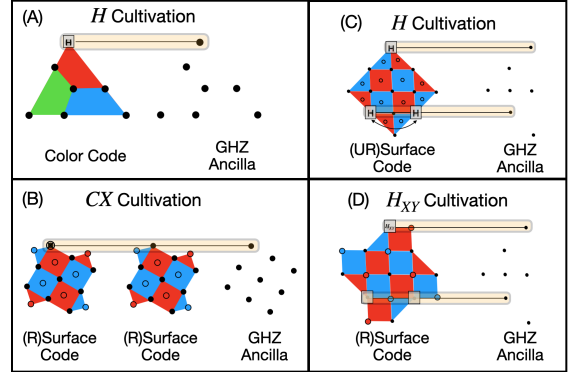


FIG. 1. H, H_{XY} and CX cultivation – Schematic diagrams of both H/H_{XY} and CX cultivation. Black dots label the data qubits, and orange rectangles label one instance of a transversal gate. (A) H cultivation on 2d triangular color code. A GHZ ancilla measures the H operator by transversal application of the controlled-Hadamard gate. (B) CX cultivation on a pair of $d = 3$ rotated surface codes. Blue and red dots label ancillas. The CX operator is measured on a pair of surface codes by transversal application of the CCX (Toffoli) gate with a GHZ ancilla as one of the controls. (C) H cultivation on the unrotated surface code, implemented using a transversal CH on all the qubits, followed by conditional SWAP along the diagonal. (D) Mid-cycle projection of the rotated surface code using the H_{XY} operator, applied using alternating CH_{XY} and \bar{CH}_{XY} gates along the diagonal and CCZ gate across the diagonal.

surement can be achieved using a *double-checking* protocol (defined in Methods), which initializes the ancilla qubits in the X basis, followed by GHZ decoding [15]. We define the logical fidelity of the protocol as the expected square amplitude of the final state projected on the target magic state, we define the acceptance rate (or simply *rate*) as the probability of accepting a shot based on the measurement results of the stabilizers and the GHZ ancilla. We describe all of these steps in more detail below.

A. Surface code cultivation

We introduce three cultivation protocols that can be applied to both the rotated surface code and unrotated surface code. We use a GHZ ancilla to measure three different transversal operations on the surface code, each involving a three qubit gate, as illustrated in Fig. 1 (B-D). These protocols are advantageous due to their operation directly on the surface code, simplifying implementation and decoding. When the entire cultivation protocol is analyzed, the advantage of working with the surface code results in a significantly higher acceptance rate compared

with color code cultivation (Fig. 1 (A)).

First, we use the H gate which is fold transversal on the unrotated surface code [23, 37]. It can therefore be implemented by applying two qubit SWAP gates along its diagonal, followed by a transversal H operator on all of the data qubits. Similarly, we can use a two-qubit CZ gate across the un-rotated surface code diagonal, combined with alternating H_{XY} and $\tilde{H}_{XY} = H_{XY}Z$ gate along the diagonal, in order to implement a transversal H_{XY} gate on the code. Conditioned on a GHZ ancilla, we can measure both H and H_{XY} operators, projecting the code into a magic state eigenfunction of these operators:

$$|T\rangle = H_{XY} |T\rangle = \left[|0\rangle + e^{i\pi/4} |1\rangle \right] / \sqrt{2} \quad (1)$$

$$|T_H\rangle = H |T_H\rangle = \cos(\pi/8) |0\rangle + \sin(\pi/8) |1\rangle \quad (2)$$

As was described in [23], at the middle of the stabilizer circuit of the rotated surface code, the stabilizer group defining the state of the code is very similar to an un-rotated surface code with the same distance. This can be used to measure the fold transversal operators of the *un-rotated* surface code on a *rotated* surface code. We utilize the decomposition of $H_{XY} = e^{-i\pi/4} SX$, and the transversal application of S and X on the rotated surface code mid-cycle (with some global phase correction). Protocols are described in more details in Methods.

We also describe CX cultivation protocol, which is applicable to any CSS code encoding a single logical qubit. In this scheme, two patches of surface codes are measured using a controlled CX operator, controlled by a GHZ ancilla. The state is then projected into the $|CX\rangle$ state:

$$|CX\rangle = |0,+\rangle + |0,-\rangle + |1,+\rangle, \quad (3)$$

B. Protocol

The full cultivation protocol consists of three stages. (1) A surface code of distance $d_1 = 3$ is initialized in the $+1$ eigenstate of all of its stabilizers, and the magic state is injected. (2) Perform a *double-check* [15] (defined in Section III B) of a GHZ state followed by a syndrome extraction round. (3) In the $d_1 = 5$ case, we expand the code into a $d_1 = 5$ surface code¹, followed by an additional *double-check*. We present this in full as psudo-code in Appendix I.

For CX cultivation, we skip the state injection. The two $d_1 = 3$ codes are fault-tolerantly initialized

in the $|+,0\rangle$ state, followed by three single CX projections. We also present results for $d_1 = 5$ with five projections, but these have a low acceptance rate.

The magic state is post-selected by measuring the GHZ ancilla and stabilizers during the protocol, and rejecting any non-trivial syndrome. This allows the logical fidelity to be limited by the code's ability for error detection. While the code is limited to $d_1 = 3$ the fidelity scales as the lowest weight undetectable error, i.e. $\propto p^3$ for some physical error parameter p . With injection and *double-check* measurement, the circuit can detect up to 3 errors. With CX cultivation, 3 CX measurements are required to achieve fault-distance 3.

Up until this point, we post select on any error in any syndrome or GHZ measurement. After the final measurement, the surface codes are expanded [5, 9, 15] to a larger code of distance $d_2 = 11$ for 10 rounds, enabling error correction to achieve higher fidelity than that of the cultivated magic state. The expansion works by initializing each newly added qubit in the basis of any weight-2 stabilizer or logical operator it extends, thus ensuring that their value stay deterministic, see [5]. At this stage, we don't post select on every syndrome, but use additional information from the decoder. The complementary gap [15, 38, 39] is the log of the ratio between probabilities of the two most likely errors that result in opposite values of the logical operator. We can set different thresholds for this value, each one giving a difference balance of the acceptance rate and fidelity. We plot all possible values of this threshold our results section.

C. Simulation

We next turn to numerical simulations. For small code distances, we use full state-vector simulations to verify the correctness of our protocol. At larger scales, beyond the reach of exact state-vector methods, we employ Clifford simulations of a similar circuit to assess the protocol's performance.

We verified the protocol's correctness by running a full state-vector simulation for both H and H_{XY} with rotated and unrotated codes with $d_1 = 3$, and for CX cultivation, we simulated a representative example of $d_1 = 2$. While we could employ the significant compute required for full-vector simulation up to $d_1 = 3$, without expansion, we could not directly estimate Similarly to [15], we observed a good agreement in both absolute fidelity and scaling, with a small factor difference, before the expansion step between the full-vector and simplified Clifford simulations. See Appendix C for details.

For the Clifford simulation [40, 41], we replaced

¹ This is similar to the color code expansion in [15].

the non-Clifford gates CCX , CCZ , $C\bar{S}WAP$, CH , CH_{XY} and $C\bar{H}_{XY}$ with combinations of CX designed to measure the logical X operators. To make sure our simulation approximates the noise in the system, we apply a uniform depolarizing noise on the the **non-Clifford** gate (which sometimes includes 3 qubits depolarizing errors, see S.I.). The results of our simulation are shown in Fig 2. Owing to its smaller qubit footprint, the rotated surface code provides the best overall fidelity, even though its circuit is longer. When idling errors are absent, the shorter circuit of the unrotated surface code performs better, as demonstrated in the next section.

Although color-code-based magic state distillation protocols [11, 15] have an initial advantage due to a smaller qubit footprint, our protocol is ultimately superior. The expansion step in our protocol is substantially more efficient than the costly grafting procedure required for color codes. Grafting requires a long idling step with high rates of post selection, necessary to convert from color code to surface code. Our protocol skips this idling step entirely, since we simply expand to a larger surface code. This results in an order-of-magnitude higher distillation rate for our protocol at representative parameters of $d_1 = 5, d_2 = 11$, which are easily comparable with previous work [15]. Our protocol is able to reach 10^{-9} infidelity with the same physical error rate $p = 10^{-3}$ and 1/5 the number of shots.

D. Efficient Cultivation with long idling time

To enable direct comparison with previous schemes, we adopt the uniform-noise model described in Ref. [15] (see Appendix A). This model treats idling as equally harmful as a two-qubit gate, which can be a reasonable approximation for certain superconducting transmon devices [42, 43]. However, some quantum devices offer significantly better idling fidelities compared to their 1Q and 2Q gates. For example, Cold atom devices have exceptionally long T_1 times while not populating the Rydberg state, and their dephasing time T_φ can be prolonged with dynamical decoupling, or by shelving in clock states [30, 31]. This bias between gates and idling can also be achieved in ions and superconducting cavities [32–34] and possible with spins in solids, like [44].

This offers a significant advantage in practice. In a recent estimate for the resources required to break RSA 2048 using superconducting qubits, roughly 20% of the qubits were designated for magic state generation [28]. Using color code cultivation and targeting 10^{-7} infidelity, the acceptance rate is approximately 5%. With $d_1 = 3$ H_{XY} cultivation we

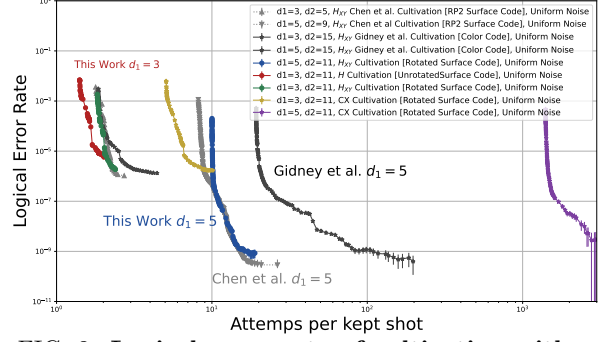


FIG. 2. **Logical error rate of cultivation with expansion - Uniform noise model** – Logical error rate, and expected attempt per kept shot of color code H cultivation by Gidney et al. [15], and surface code CX, H_{XY} and H cultivation. The physical error rate is $p = 10^{-3}$ using uniform noise model. The schemes expand into a larger surface codes with very similar performance [15]; The color code is expanded to a grafted surface code, while the rest expand to a standard surface codes, all with distance d_2 . The different points label various thresholds for the complementary gap post-selection. Error bars represent a single standard deviation. We included the $d_1 = 5$ CX case although it has large error bars, giving only an approximate bound on its error rate.

have roughly 75% acceptance rate with fewer qubits (because of the smaller final distance) and roughly half the number of rounds. In total, this results in over an order of magnitude reduction in qubit-rounds cost.

Still, in a resource estimate designed specifically for cold atoms [27], magic-state cultivation occupies half the atoms during addition (where most of the Toffoli gates are consumed). Our short circuit and 75% acceptance rate together would reduce the qubit-rounds assumed in [27] by over a factor of $\times 20$. This would directly reduce the qubit count during addition by over 6 million qubit (or roughly 40%).

E. Erasure Qubits and Loss

Erasure qubits [45–50] are a type of qubits with a specific noise mechanism that can be directly identified. In superconducting qubits, energy relaxation events can be identified by encoding a single qubit in the single excitation subspace of two transmons [46] or cavities [51, 52], and measuring the zero excitation state. In Rydberg atoms [49, 53, 54], during a two qubit gate the population in the Rydberg state decays to many states, most of them outside of the computational subspace. Observing the population in these states identifies this decay. Similarly, loss in Rydberg atoms can be detected through destructive measurements [30, 55]. In the context of cultivation, any technique that identifies loss by the end of

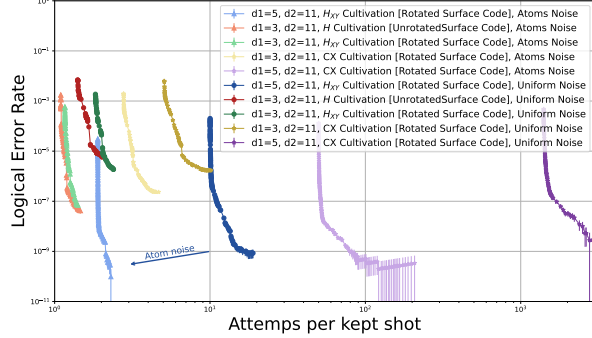


FIG. 3. Logical error rate of cultivation with expansion - Atom noise model – Logical error rate and acceptance rate of surface code CX , H_{XY} and H cultivation with Uniform and Atom noise model. In the Atom noise model, idling doesn't introduce any additional error, which approximate the effect of dynamical decoupling or shelving in clock-states. The physical error rate is $p = 10^{-3}$, and the full noise model is defined in S.I. For practical application that utilize synthillation, achieving 10^{-7} infidelity is possible with $d_1 = 3$ and approximately 75% rate.

the protocol effectively functions as erasure detection [55].

It is a standard classical result [56] that the fault distance of erasure for error *correction* is d , which generalizes to quantum codes [49, 50]. Accordingly, cultivation error rates are expected to scale as p^{d_1} .² Importantly, the fault distance of erasure for error *detection* is ∞ , assuming erasure can always be detected. The erasure rate doesn't effect the logical fidelity [35] as long as it can be detected. In this limit, only the acceptance rate is affected by erasure. Since most Pauli errors are identifiable to begin with [35], the effect of erasure e is approximately to reduce the acceptance rate to the rate of the same circuit with only Pauli noise with rate $p = e$. See Methods for our analysis and [35], for a detailed investigation of this trade off.

We estimated the effect of erasure on cultivation by estimating its effect on acceptance rate without the expansion step in Fig. 4. In the Methods section, we provide an explanation of the estimation process for assessing the impact of erasure on complementary gap decoding. It is clear that the overhead of adding $e = 2 \times 10^{-3}$ erasure for $d_1 = 3$ surface code cultivation roughly reduces the acceptance rate by a factor of 5. If in this regime one can achieve a meaningful bias, resulting in $p = 10^{-4}$,

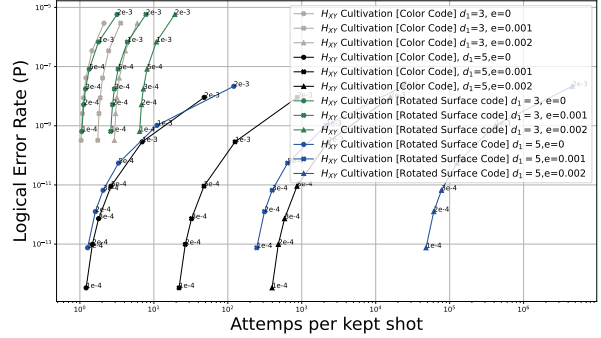


FIG. 4. Logical error rate and Acceptance rate of erasure Qubits – Logical error rate and acceptance rate of erasure qubits used for the initialization step of cultivation. The points are labeled by the residual Pauli error rate p . As mentioned in the main text, the logical error rate does not depend on the erasure rate but only on the residual Pauli error rate. Importantly, the color-code expansion step is considerably more expensive than for the surface code, but isn't shown in this plot (see Methods). Still, from this graph we can extract the tradeoff when converting between different erasure and Pauli rates. For example, if $p = 10^{-3}$ can be converted to $e = 2 \times 10^{-3}$ and $p = 10^{-4}$, it would reduce the acceptance rate of $d_1 = 3$ cultivation by roughly a factor of 5, but improve the fidelity by over 10^3 .

it can reach infidelity of 10^{-9} with the same rate as $d_1 = 5, p = 10^{-3}$ cultivation but with significantly fewer qubits and a shorter protocol. Such a level of bias is realistic for certain trapped-atom species [49] and for superconducting qubits [48], although the latter would require some degree of long-range connectivity.

If the bias is small, which is the case for some trapped atom species [30] where loss represent about 50% of gate fidelity, cultivation is still improved by loss detection. The rate would be the same as we described before, but the final fidelity would improve by roughly 2^{d_1} , which as seen in Fig 4 is between 8 – 50 depending on the specific protocol.

If the bias can reach $e = 10^{-3}$ and $p = 10^{-4}$ with only local connectivity, such as for dual-rail superconducting qubits [46, 48], it would be possible to achieve $p_L \approx 10^{-15}$ once every 200 attempts with $d_1 = 5$ color code cultivation of [15], if we include post selection on the complementary gap. At this scale, the qubit-cycles count of cultivation is 1.5×10^5 ³, which is about 20 times less than the $(15\text{-to-}1)^6_{13,5,5} \times (15\text{-to-}1)^6_{29,11,13}$ scheme of [7] using

² This approximation can fail for $d_1 = 5$ at very small p , since a small number of weight-4 undetectable errors can arise from hook errors in the expansion step from $d_1 = 3$ [15].

³ This is the qubit-cycles count of H cultivation with $p_0 = 10^{-3}$ as reported in [15]. In the erasure case, we assume the erasure overhead of Pauli and erasure are the same, and the additional $p = 10^{-4}$ Pauli errors have minimal additional overhead [35]. Since gap-estimation of erasure scales better

non-erasure qubits.

Erasure offers an additional interesting opportunity for cultivation, which is to reach algorithmic interesting infidelities with only a $d_1 = 2$ unrotated surface code and a single GHZ projection. This protocol requires only 9 physical qubits. With this setup and a residual Pauli error rate of $p = 10^{-4}$, cultivation can achieve a state infidelity of 10^{-6} , which can then be combined with synthillation [57] to reach algorithmically relevant fidelity. For more information, see the S.I.

III. METHODS

A. H , H_{XY} and CX Cultivation

The unrotated surface code is fold-dual [23, 37]. Therefore, applying a transversal Hadamard gate followed by the SWAP duality applies the Hadamard gate on the logical operators (Fig. 1), and permutes the stabilizers along the duality. For cultivation, all of the stabilizers are initialized in the $+1$ subspace, which means this operation acts trivially on the stabilizers of the code, and only affects the logical operator.

Similarly, applying alternating S and S^\dagger gates along the diagonal of the unrotated surface code, and applying CZ gates orthogonally on the non-diagonal qubits (Fig. 1), leaves the stabilizers in the $+1$ subspace unchanged, while applying a logical S gate on the code (or a logical S^\dagger gate, if the order is reversed). Similarly, applying a physical X gate on all the qubits along the diagonal applies a logical X gate. Together, we can use the identities:

$$H_{XY} = e^{-i\frac{\pi}{4}} SX \quad (4)$$

$$\bar{H}_{XY} = e^{i\frac{3\pi}{4}} S^\dagger X = H_{XY} Z \quad (5)$$

Which together demonstrate that we can apply alternating H_{XY} , \bar{H}_{XY} gates on the diagonal and CZ gates off the diagonal to get a logical H_{XY} gate on the unrotated surface code.

The same idea is applicable on the rotated surface code, using its mid-cycle state. At the middle of the rotated surface code syndrome extraction circuit, the state of the code morphs into the unrotated surface code state [23, 58], which allows us to use the same transversal gates described above. This way, in a single round, both its stabilizers and logical state can be measured using standard ancillas and an additional GHZ ancilla.

than Pauli noise, this result should be understood as the bounds on qubit-cycles count.

Lastly, we describe the CX cultivation as measurement of the CX operator on a pair of codes. This procedure is applicable to any CSS code encoding a single logical qubit. By measuring the transversal CX operator of two logical qubit, as in Fig. 1, both are projected from the initial state $|+, 0\rangle$, which can be easily initialized, onto the following state:

$$|CX\rangle = |0, +\rangle + |0, -\rangle + |1, +\rangle, \quad (6)$$

where $|0\rangle, |1\rangle$ label the $1, -1$ eigenstates in the Pauli Z basis, and $|+\rangle, |-\rangle$ label the $1, -1$ eigenstates in the Pauli X basis.

It is known [8, 14] that the state $|CZ\rangle = |00\rangle + |01\rangle + |10\rangle$ is a magic state, in the sense that two copies of the $|CZ\rangle$ state can be fault tolerantly converted to a single Toffoli state with probability $4/9$ [8, 14]. The $|CX\rangle$ state differs from the $|CZ\rangle$ state by a single H operator, so it is easy to convert between them.

B. Phase Kickback and Double Checking

We measure the state using a GHZ ancilla with two different methods: phase kickback and *double-checking*. For phase-kickback we initialize a GHZ ancilla by expanding a $|+\rangle$ state from one qubit using CX gates. Then, a controlled transversal gate is applied with the GHZ state as control.

In general, we label the logical transversal operation by A , which can be achieved by transversal application of a set of operations $\{A_i\}$ (where i can label a single qubit or pairs of qubits, depending on the specific transversal operation). Our operator has two eigenvalues ± 1 , and we label two state with these eigenvalues as follows: $A|\pm A\rangle = \pm|\pm A\rangle$.

If the logical qubits starts in some superposition of the two eigenstates $|\psi\rangle = \alpha|+A\rangle + \beta|-A\rangle$, the application of the transversal operation conditioned on the GHZ ancilla results in the following state:

$$\left(\prod_i CA_i \right) \left[\frac{|0\rangle^{\otimes n} + |1\rangle^{\otimes n}}{\sqrt{2}} \right] |\psi\rangle = \alpha \left[|0\rangle^{\otimes n} + |1\rangle^{\otimes n} \right] |+A\rangle + \beta \left[|0\rangle^{\otimes n} - |1\rangle^{\otimes n} \right] |-A\rangle$$

Where CA_i is a transversal A_i gate conditioned on the i 'th ancilla in the GHZ state, see Fig 5. Running the circuit generating the GHZ in reverse and then measuring its qubits effectively measures the GHZ state and can identify a single bit flip error [11].

Note that if the transversal operation did not act trivially on the stabilizers of the code, it would generate additional entanglement between the code state and the ancilla. In such a case, the superposition of the ancilla would be destroyed, leaving it in

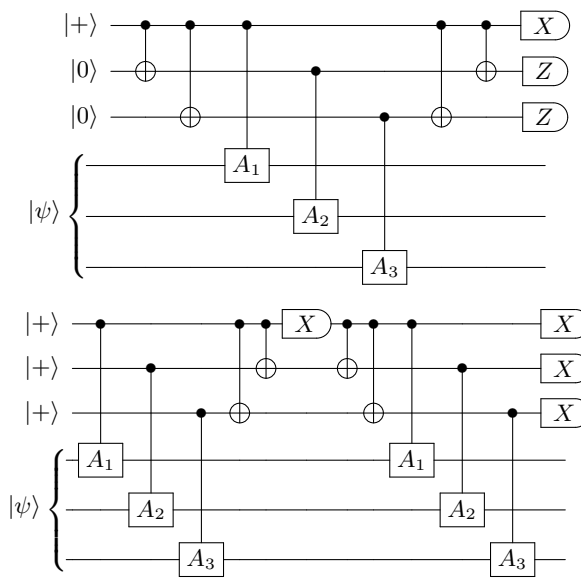


FIG. 5. Schematic description of phase-kickback and double-checking using a GHZ ancilla

The top 3 Qubits represent the GHZ ancilla, while the bottom 3 Qubits represent the surface code (or codes)

we project. Both circuits projects $|\psi\rangle$ to the $+1$ eigenvector of A when all measurement outcomes are $+1$. The state is discarded if any measurement outcome is -1 . (Top) schematic diagram of a phase-kickback measurement of a transversal A operator using a GHZ ancilla. (Bottom) Schematic diagram of a *double-checking* circuit projecting the A operator twice.

a mixed state over $|0\rangle^{\otimes n}$ and $|1\rangle^{\otimes n}$. A subsequent measurement would then fail to reveal any information about the state of the code.

In the *double-checking* protocol, first introduced in [15], all the ancilla qubits are initialized in the $|+\rangle$ state. The controlled transversal operation is applied, which puts the ancilla in the following superposition:

$$\begin{aligned} \left(\prod C A_i \right) |+\rangle^{\otimes n} \otimes |\psi\rangle = \alpha \prod (|0\rangle + |1\rangle A_i) |+A\rangle \\ + \beta \prod (|0\rangle + |1\rangle A_i) |-A\rangle \end{aligned} \quad (7)$$

Notice that $\prod (|0\rangle + |1\rangle A_i) |\pm A\rangle$ is a ± 1 eigenstate of the $X^{\otimes n}$ operator on the ancilla. Measuring the $X^{\otimes n}$ operator of the ancilla would then recover the eigenvalue of A . This is done by running the GHZ-generating circuit in reverse, which moves the information into a specific qubit that is then measured in the X basis. *Double-checking* is achieved by then running the circuit in reverse and measuring all of the ancilla qubits in the X basis, see Fig 5

C. Fault tolerance

CX measurement has different fault tolerance properties than H/H_{XY} measurement. In the H/H_{XY} measurement schemes, the magic state is initially injected into the code (Appendix H), making any following measurement deterministic (absent any errors). The fault distance, i.e., the minimal number of errors that cause an undetectable error⁴, is limited either by the distance of the code, or by one more than the number of H projections. This is because the injection step must fail in addition to all subsequent H projections.

We assume here that the syndrome extraction circuits do not introduce any hook errors, which is true for the surface code, flagged color-code [11] and the fold transversal gates [23]. If the code is protected by error correction using the stabilizers, the fault distance is the standard $t_1 = \lfloor (d_1 + 1)/2 \rfloor$. If the code is protected by post-selecting on any stabilizer flip, the fault distance becomes the full error detection distance d_1 . Therefore, the H projection should be repeated either $t_1 - 1$ for error correction, or $d_1 - 1$ times for error detection with post-selection.

Generally, injection improves the rate by reducing the number of required H/H_{XY} measurements by 1 and making them deterministic. It is similarly possible to inject a $|CX\rangle$ state at the beginning of the cultivation procedure, but some errors at that stage would not be identifiable later, reducing the fault-distance to 1. For example, a failed injection that resulted in the state $|0, +\rangle$ would not be detected by any subsequent CX measurement.

Instead, for CX cultivation, the two surface codes are fault-tolerantly initialized in the $|+, 0\rangle$ state by initializing each physical qubit in the $|+\rangle$ and $|0\rangle$ states, respectively, and measuring all stabilizers (see Appendix H). Single qubit gates are then applied to set all the stabilizers to the $+1$ subspace. The transversality of CCX means that the logical measurement is fault tolerant. The CX measurement is repeated d_1 times, and the state is discarded following any detection event. The initial measurement projects the state to the $|CX\rangle$ state with probability $3/4$, and any subsequent measurement is deterministic (again, absent any errors). In this way, the CX scheme has a fault distance d_1 , at the expense of an additional CX measurement and non-deterministic initialization.

⁴ In general, the fault distance depends on the specific noise model. We follow a standard assumption where n -qubit gates are followed by n -qubit error terms with the same support.

For the same reason, the codes cannot grow during the CX cultivation stage. The CX measurement projects into a subspace which contains multiple states, so some weight 3 errors aren't identifiable in the $d = 5$ state. For example, consider a logical Z error on the control qubit during the $d_1 = 3$ stage. This error has weight 3, but it will not be identifiable by a subsequent $d_1 = 5$ CX measurement, as it commutes with CX . To achieve fault distance of 5, the surface codes should be initialized and measured at $d_1 = 5$ for the entire cultivation protocol.

The distance of the final expanded code should be chosen such that cultivation is the dominant error mechanism. This is the correct optimization when magic states are consumed directly for computation, but not when their fidelity is subsequently improved through distillation or synthillation. We chose to simulate with $d_2 = 11$, which yields a code with an error rate comparable to that in [15], while offering the advantage of correcting up to five errors. This level of protection ensures that the weight-5 errors introduced during cultivation dominate the final fidelity. In principle, none of our figures would change if we used $d_2 = 5$ or $d_2 = 15$ instead, since our simulation always allows for post-selection based on the complementary gap.

IV. CLIFFORD SIMULATION

For the Clifford benchmark of our protocol, we simulated a slightly different protocol composed only of Clifford gates [15, 40, 41, 59]. We replaced the non-Clifford controlled-gates with combinations of CX chosen to measure the logical X operator. Importantly for H and H_{XY} cultivation schemes, the support of the CX is not the full code but only most of the qubits. Our full vector simulation demonstrates that this effect is relatively small.

For H and H_{XY} cultivation schemes, our Clifford circuit measures the X operator instead. On the unrotated surface code, this operator can be accessed by measuring the X operator on all the data qubits except the corners, and this is the operator our simulation measures. For CX cultivation, our protocol measures the XX operator on two surface codes. Just like the CX projection, the XX measurement projects a pair of codes into a subspace with an additional degree of freedom, the ZZ operator, and not to a specific state like H and H_{XY} cultivation schemes. We probe the effect of 3-body interactions by introducing 3-body noise terms (see below) following the CX operations, along the support of what would have been the non-Clifford gate, see Fig. 1.

For the surface code, our protocol initializes a $|+\rangle$ state and applies a non-fault tolerant Z or X rotation to

inject the magic state (see Appendix H for details). For the Clifford simulation, we applied the entire injection circuit apart from the rotation, which leaves the state in the same state (but introduces weight 1 logical errors). For CX cultivation, two surface codes are initialized in the $|+, 0\rangle$ state. We then apply a transversal CX gate between them that results in a $+1$ eigenstate of both of their common logical X_1X_2 and Z_1Z_2 operators. We then apply a logical Z_1 operator with probability $1/4$, which simulates the probabilistic nature of the initial CX projection.

The projection circuit of both H_{XY} and CX cultivation are shown in Fig. 7 and Fig. 8. In both, the non-Clifford operation is replaced by some CX 's.

At the end of the simulation, the X operator is measured perfectly. For CX cultivation, both XX and ZZ are measured. The log-likelihood of the matching for all four possible values of XX and ZZ is evaluated, and the most likely option is chosen. The complementary gap is defined as the difference between the two most likely options. The ZZ operator is not measured during the protocol, but its initialization is fault-tolerant. This corresponds to the additional degrees of freedom of the $+1$ subspace of CX that are not probed by the GHZ measurement, but are initialized fault-tolerantly.

We introduce depolarizing channels as noise as defined in Appendix A. For the Atom noise model, only removed the idling noise from the noise model B. Additional 3-qubit errors are injected during 3-qubit non-Clifford operations, to approximate the implementation of a 3-qubit gate by composing multiple noisy 1Q and 2Q gates[60]. Further details are presented in the Appendix (Sec. G).

The expansion step of surface-code cultivation is simpler due to the shape of the code; Color code based cultivation requires lattice surgery [12, 13] or grafting [15] to transform the code into a surface code, both of which are quite costly. Here, we follow the same expansion as in [5].

V. CULTIVATION WITH ERASURE QUBITS

The benefit of using erasure qubits for cultivation is estimated analytically by assuming perfect detection and estimating the resulting acceptance rate. Any missed detection can be regarded as an additional Pauli error simply depolarizing the erased gate without a signal, which we assume for measurement error q , erasure rate e and Pauli rate p obeys $eq \ll p$. To simulate erasure, we define the Pauli noise level by a parameter p , as defined in Appendix A. At every noise location, we introduce additional erasure error with probability e . We assume the state is

post-selected out following every erasure error.

Fig. 4 shows the acceptance rate for cultivation on both the surface code for various values of p, e , in a system with erasure bias. To compare the benefit of erasure qubits, we assume there is some additional cost associated with erasure detection [50]. A non-erasure qubit circuit with Pauli error rate p_0 , is compared to an erasure circuit with erasure e and Pauli rate p with more overall noise ($p + e > p_0$) and bias for erasure ($p \ll p_0$). For a non-erasure qubit with Pauli rate $p_0 = 10^{-3}$, we can compare to $e \in \{1 \times 10^{-3}, 2 \times 10^{-3}\}$ erasures and $p = 10^{-4}$ residual Pauli noise. For $e = 2p_0$, we say that the "overhead" due to erasure conversion is two, and we see in Fig. 4 that the effect on $d_1 = 3$, H_{XY} surface code cultivation is to reduce the rate by a factor of 5. At this cost, the logical fidelity improves by $\sim (p/p_0)^{d_1} \approx 10^3$. The acceptance rate decays exponentially in both qubit count and erasure rate. Therefore, doubling the erasure rate squares the required shots.

We found the expansion stage very difficult to probe numerically. Introducing erasure into circuits for decoding requires generating a new matching graph for each circuit, which is costly. It is possible to probe higher noise rates which increase the logical error rates, and would then require fewer shots to estimate, but that too required too many shots due to the increased post-selection rate.

A coarse but informative estimate of the post-selection overhead associated with the expansion step can be obtained by comparing the relative overhead between the initialization and final gap-estimation stages for the case $p = e$. This approach assumes that erasure errors have, on average, a comparable effect on gap decoding, while allowing for a much simpler numerical evaluation. When combined with the initialization acceptance rates presented in Fig. 4, this approximation provides a lower bound on the overall cultivation rate under erasure-biased noise. It is reasonable to assume erasure errors result in higher overall logical fidelity at the expense of less post-selection on the complementary gap. Erasure errors convey more information that can be utilized by the decoder (which is why the erasure threshold is much higher than the Pauli threshold for circuit model noise [46]).

In order to demonstrate this effect, we used a simpler model that does not include post-selection on the stabilizers. A standard surface-code memory experiment is post-selected using only the complementary gap following d rounds, with various values of erasure probability e and Pauli noise p in the same manner described earlier. The noise model is defined in Appendix A. As can be seen in Fig. 6, even when $e = 2p$, the gap estimation can identify a

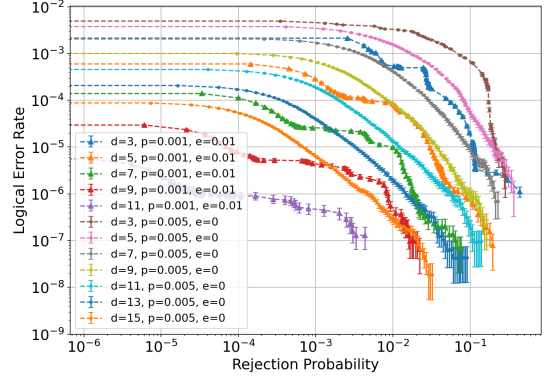


FIG. 6. **Logical error rate and rejection probability of surface code memory experiment** – Logical error rate of d rounds memory experiments. Different points label different threshold for the complementary gap. We compare two different regimes, one with only Pauli noise and one with mix of erasure and Pauli noise obeying $e = 2p$. When erasure dominates the noise model, it can achieve the same logical fidelity and significantly higher rate with a factor of 2 overhead.

correct decoding much more easily.

VI. DISCUSSION

In this work, we demonstrated how cultivation can be implemented directly on the surface code using non-local connection. Although the initialization step of cultivation on the surface code has a slightly lower rate compared with color-code cultivation, this effect is compensated by the simple and high rate expansion step of the surface code to higher distances. This is clearly superior in architectures with all-to-all connectivity such as cold atoms and trapped ions. Even with architectures exhibiting limited long-range connectivity (e.g., superconducting qubits [61]), compiling non-local interactions will be quite efficient, given their small number.

The acceptance rate can be further improved by using additional information for the decoder, similar to [29]. In our analysis, we used similar assumptions about the speed of the decoder to [15]. We simulated 10 additional rounds of syndrome extraction before we considered the cultivated state ready. This approximates a $10\mu\text{s}$ delay in superconducting qubits. This assumption has a significant effect on the qubit-round metric, since in architectures with slower measurement time, there would be no decoder delay. Although in practice that would make cultivation slower, in terms of qubit-round cost that can make cultivation appear cheaper. A direct compari-

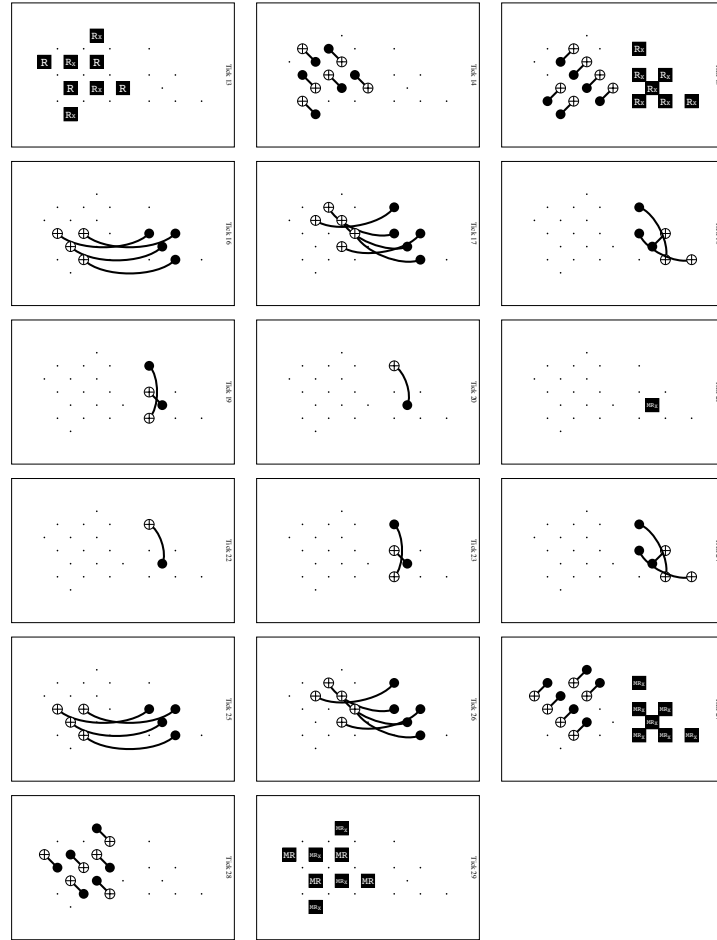


FIG. 7. **Circuit measuring the X operator on a rotated surface code mid SE cycle** – A *double-check* of the X operator on a rotated surface code with $d_1 = 3$ mid SE cycle. From top to bottom, left to right, each panel represent a time slice of the circuit (labeled with tick index). For non-Clifford simulation, the CX 's in ticks (16,17,25,26) were replaced with CCZ , CH_{XY} and $C\bar{H}_{XY}$

[Click here to view in Crumble](#)

son would account for transport and 2Q gate times, which isn't well captured by the qubit-round metric, which is why we did not include it here. We leave this analysis for future work.

Many quantum computing architectures have high idling fidelity. As we have shown, this gives a great benefit for magic state cultivation, both in fidelity and rate. For example, running 2048 bit RSA only requires roughly $10^{-7} T$ gate infidelity [27, 28], which can be achieved with $d_1 = 3$ cultivation on cold atoms with very minimal loss detection. Since prior work assumed cultivation was successful with such small probability, it either required idling until the magic states are ready [28], or significantly increasing the number of qubits [27]. Our high rates suggest magic states can be generated highly efficiently, which would have very large effect on previ-

ous resource estimates.

VII. ACKNOWLEDGMENTS

We thank Craig Gidney for suggesting the mid-cycle measurement of the H_{XY} operator, and for making Stim, Sinter and Crumble [41] open source, all of which were instrumental for this project.

The authors were made aware of two related publications posted on arXiv concurrently with this work: one from Puri's group, which investigates fold transversal cultivation on the surface code [62], and another from J. Claes, which demonstrates surface code cultivation using two-qubit gates [63].

We thank the staff from across the AWS Center for Quantum Computing that enabled this project. We

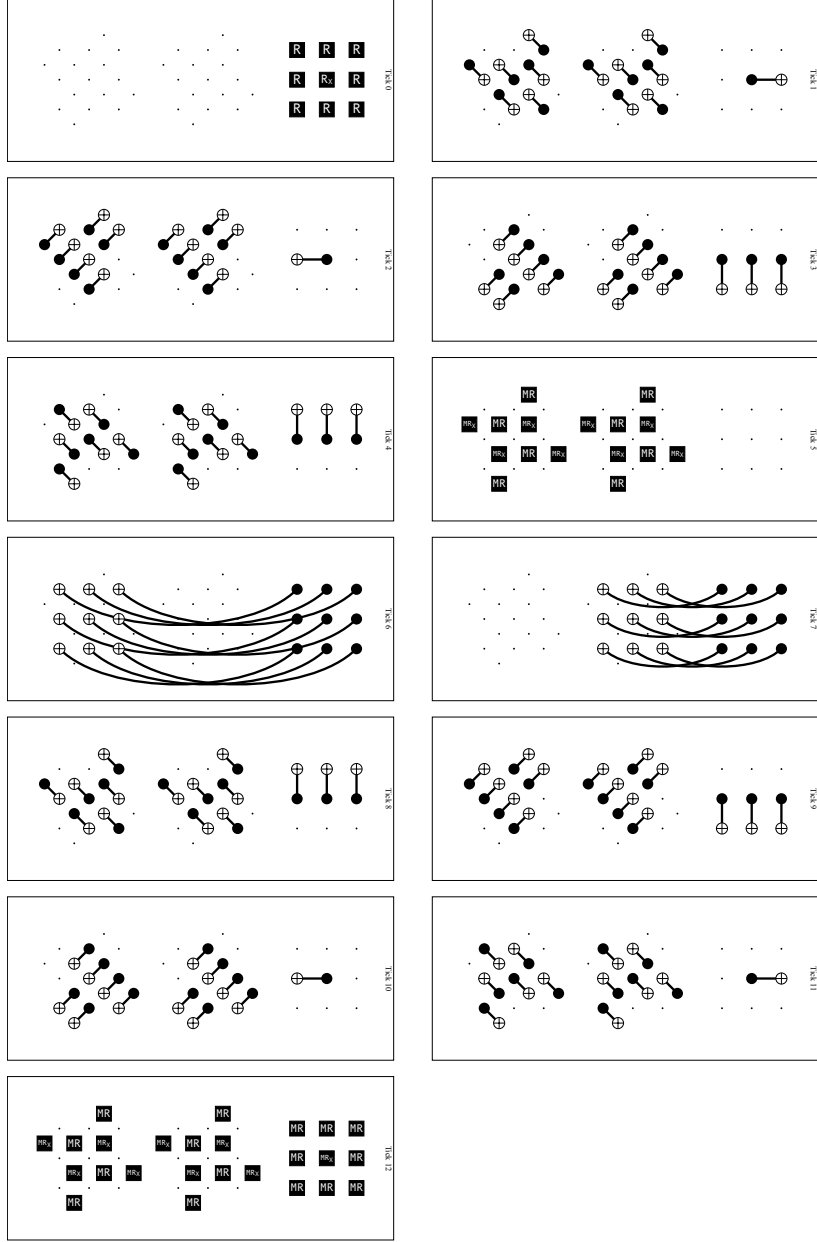


FIG. 8. **Circuit measuring the XX operator** – A GHZ measurement of the XX operator on a pair of surface codes. From top to bottom, left to right, each panel represent a time slice of the circuit (labeled with tick index). During the collapse and expansion stages of the GHZ state, the two surface codes are performing their respective stabilizer measurements. To measure CX , Ticks 6-7 should show a transversal CCX gates instead of CXX .

[Click here to view in Crumble](#)

also thank Simone Severini, James Hamilton, Nafea Bshara, and Peter DeSantis at AWS, for their involvement and support of the research activities at the AWS Center for Quantum Computing.

VIII. CIRCUITS AND DATA

The circuits, decoders and data are available in [\[64\]](#).

[1] D. Aharonov and M. Ben-Or, in *Proceedings of the twenty-ninth annual ACM symposium on Theory of computing* (1997) pp. 176–188.

[2] E. Knill, R. Laflamme, and W. H. Zurek, *Science* **279**, 342 (1998).

[3] B. Eastin and E. Knill, *Physical review letters* **102**, 110502 (2009).

[4] L. Lao and B. Criger, in *Proceedings of the 19th ACM International Conference on Computing Frontiers* (2022) pp. 113–120.

[5] C. Gidney, arXiv preprint arXiv:2302.12292 (2023).

[6] S. Bravyi and J. Haah, *Physical Review A—Atomic, Molecular, and Optical Physics* **86**, 052329 (2012).

[7] D. Litinski, *Quantum* **3**, 205 (2019).

[8] E. Dennis, *Physical Review A* **63**, 052314 (2001).

[9] H. Goto, *Scientific Reports* **4**, 7501 (2014).

[10] H. Goto, *Scientific reports* **6**, 19578 (2016).

[11] C. Chamberland and K. Noh, *npj Quantum Information* **6**, 91 (2020).

[12] T. Itogawa, Y. Takada, Y. Hirano, and K. Fujii, *Bulletin of the American Physical Society* (2024).

[13] Y. Hirano, T. Itogawa, and K. Fujii, arXiv preprint arXiv:2404.09740 (2024).

[14] R. S. Gupta, N. Sundaresan, T. Alexander, C. J. Wood, S. T. Merkel, M. B. Healy, M. Hillenbrand, T. Jochym-O’Connor, J. R. Wootton, T. J. Yoder, *et al.*, *Nature* **625**, 259 (2024).

[15] C. Gidney, N. Shutty, and C. Jones, arXiv preprint arXiv:2409.17595 (2024).

[16] H. Bombin and M. A. Martin-Delgado, *Physical review letters* **97**, 180501 (2006).

[17] A. Kubica, B. Yoshida, and F. Pastawski, *New Journal of Physics* **17**, 083026 (2015).

[18] C. Gidney and C. Jones, arXiv preprint arXiv:2312.08813.

[19] S. B. Bravyi and A. Y. Kitaev, arXiv preprint quant-ph/9811052 (1998).

[20] E. Dennis, A. Kitaev, A. Landahl, and J. Preskill, *Journal of Mathematical Physics* **43**, 4452 (2002).

[21] A. Y. Kitaev, *Annals of physics* **303**, 2 (2003).

[22] O. Higgott, *ACM Transactions on Quantum Computing* **3**, 1 (2022).

[23] Z.-H. Chen, M.-C. Chen, C.-Y. Lu, and J.-W. Pan, arXiv preprint arXiv:2412.01391 (2024).

[24] M. Saffman, T. G. Walker, and K. Mølmer, *Reviews of modern physics* **82**, 2313 (2010).

[25] H. Levine, A. Keesling, G. Semeghini, A. Omran, T. T. Wang, S. Ebadi, H. Bernien, M. Greiner, V. Vuletić, H. Pichler, *et al.*, *Physical review letters* **123**, 170503 (2019).

[26] S. J. Evered, D. Bluvstein, M. Kalinowski, S. Ebadi, T. Manovitz, H. Zhou, S. H. Li, A. A. Geim, T. T. Wang, N. Maskara, *et al.*, *Nature* **622**, 268 (2023).

[27] H. Zhou, C. Duckering, C. Zhao, D. Bluvstein, M. Cain, A. Kubica, S.-T. Wang, and M. D. Lukin, in *Proceedings of the 52nd Annual International Symposium on Computer Architecture* (2025) pp. 1432–1448.

[28] C. Gidney, arXiv preprint arXiv:2505.15917 (2025).

[29] Z.-H. Chen, M.-C. Chen, C.-Y. Lu, and J.-W. Pan, arXiv preprint arXiv:2503.18657 (2025).

[30] D. Bluvstein, A. A. Geim, S. H. Li, S. J. Evered, J. Ataides, G. Baranes, A. Gu, T. Manovitz, M. Xu, M. Kalinowski, *et al.*, arXiv preprint arXiv:2506.20661 (2025).

[31] H. J. Manetsch, G. Nomura, E. Bataille, K. H. Leung, X. Lv, and M. Endres, *arXiv preprint arXiv:2403.12021* (2025), arXiv:2403.12021 [quant-ph].

[32] C. Ryan-Anderson, N. C. Brown, M. S. Allman, B. Arkin, G. Asa-Attuah, C. Baldwin, J. Berg, J. G. Bohnet, S. Braxton, N. Burdick, J. P. Campora, A. Chernoguzov, J. Esposito, B. Evans, D. Francois, J. P. Gaebler, T. M. Gatterman, J. Gerber, K. Gilmore, D. Gresh, A. Hall, A. Hankin, J. Hostetter, D. Lucchetti, K. Mayer, J. Myers, B. Neyenhuis, J. Santiago, J. Sedlacek, T. Skripka, A. Slatton, R. P. Stutz, J. Tait, R. Tobey, G. Vittorini, J. Walker, and D. Hayes, “[Implementing fault-tolerant entangling gates on the five-qubit code and the color code](#),” (2022), arXiv:2208.01863 [quant-ph].

[33] C. Ryan-Anderson, J. G. Bohnet, K. Lee, D. Gresh, A. Hankin, J. P. Gaebler, D. Francois, A. Chernoguzov, D. Lucchetti, N. C. Brown, T. M. Gatterman, S. K. Halit, K. Gilmore, J. A. Gerber, B. Neyenhuis, D. Hayes, and R. P. Stutz, *Phys. Rev. X* **11**, 041058 (2021).

[34] T. LeBlond, P. Groszkowski, J. G. Lietz, C. M. Seck, and R. S. Bennink, “[Logical error rates for the surface code under a mixed coherent and stochastic circuit-level noise model inspired by trapped ions](#),” (2025), arXiv:2508.14227 [quant-ph].

[35] S. Jacoby, Y. Vaknin, A. Retzker, and A. L. Grimsmo, *arXiv preprint arXiv:2504.02935* (2025).

[36] C. Chamberland, K. Noh, P. Arrangoiz-Arriola, E. T. Campbell, C. T. Hann, J. Iverson, H. Putteman, T. C. Bohdanowicz, S. T. Flammia, A. Keller, *et al.*, *PRX Quantum* **3**, 010329 (2022).

[37] N. P. Breuckmann and S. Burton, *Quantum* **8**, 1372 (2024).

[38] H. Bombín, M. Pant, S. Roberts, and K. I. Seetharam, *PRX Quantum* **5**, 010302 (2024).

[39] C. Gidney, M. Newman, P. Brooks, and C. Jones, arXiv preprint arXiv:2312.04522 (2023).

[40] S. Aaronson and D. Gottesman, *Physical Review A—Atomic, Molecular, and Optical Physics* **70**, 052328 (2004).

[41] C. Gidney, *Quantum* **5**, 497 (2021).

[42] A. Hashim, R. K. Naik, A. Morvan, J.-L. Ville, B. Mitchell, J. M. Kreikebaum, M. Davis, E. Smith, C. Iancu, K. P. O’Brien, *et al.*, arXiv preprint arXiv:2010.00215 (2020).

[43] B. Foxen, C. Neill, A. Dunsworth, P. Roushan, B. Chiaro, A. Megrant, J. Kelly, Z. Chen, K. Satzinger, R. Barends, *et al.*, *Physical Review Letters* **125**, 120504 (2020).

- [44] P. Steinacker, N. D. Stuyck, W. H. Lim, T. Tanttu, M. Feng, A. Nickl, S. Serrano, M. Candido, J. D. Cifuentes, F. E. Hudson, *et al.*, arXiv preprint arXiv:2410.15590 (2024).
- [45] S. Bartolucci, P. Birchall, H. Bombin, H. Cable, C. Dawson, M. Gimeno-Segovia, E. Johnston, K. Kieling, N. Nickerson, M. Pant, *et al.*, *Nature Communications* **14**, 912 (2023).
- [46] A. Kubica, A. Haim, Y. Vaknin, H. Levine, F. Brandão, and A. Retzker, *Physical Review X* **13**, 041022 (2023).
- [47] A. Retzker and A. Kubica, US patent US20240104416A1 (2024).
- [48] H. Levine, A. Haim, J. S. Hung, N. Alidoust, M. Kalaee, L. DeLorenzo, E. A. Wollack, P. Arrangoiz-Arriola, A. Khalajhedayati, R. Sanil, *et al.*, *Physical Review X* **14**, 011051 (2024).
- [49] Y. Wu, S. Kolkowitz, S. Puri, and J. D. Thompson, *Nature communications* **13**, 4657 (2022).
- [50] S. Gu, Y. Vaknin, A. Retzker, and A. Kubica, arXiv preprint arXiv:2408.00829 (2024).
- [51] K. S. Chou, T. Shemma, H. McCarrick, T.-C. Chien, J. D. Teoh, P. Winkel, A. Anderson, J. Chen, J. C. Curtis, S. J. de Graaf, *et al.*, *Nature Physics* **20**, 1454 (2024).
- [52] A. Koottandavida, I. Tsoutsios, A. Kargioti, C. R. Smith, V. R. Joshi, W. Dai, J. D. Teoh, J. C. Curtis, L. Frunzio, R. J. Schoelkopf, *et al.*, *Physical Review Letters* **132**, 180601 (2024).
- [53] S. Ma, G. Liu, P. Peng, B. Zhang, S. Jandura, J. Claes, A. P. Burgers, G. Pupillo, S. Puri, and J. D. Thompson, *Nature* **622**, 279 (2023).
- [54] P. Scholl, A. L. Shaw, R. B.-S. Tsai, R. Finkelstein, J. Choi, and M. Endres, *Nature* **622**, 273 (2023).
- [55] G. Baranes, M. Cain, J. Ataides, D. Bluvstein, J. Sinclair, V. Vuletic, H. Zhou, and M. D. Lukin, arXiv preprint arXiv:2502.20558 (2025).
- [56] F. MacWilliams, Elsevier Science Publishers BV google schola **2**, 39 (1977).
- [57] C. Jones, *Physical Review A* **87** (2013), [10.1103/physreva.87.022328](https://doi.org/10.1103/physreva.87.022328).
- [58] M. Vasmer and A. Kubica, *PRX Quantum* **3**, 030319 (2022).
- [59] D. Gottesman, arXiv preprint quant-ph/9807006 (1998).
- [60] M. AbuGhanem, arXiv preprint arXiv:2501.02222 (2025).
- [61] Z. He, A. Cowtan, D. J. Williamson, and T. J. Yoder, arXiv preprint arXiv:2503.10390 (2025).
- [62] K. Sahay, P.-K. Tsai, K. Chang, Q. Su, T. B. Smith, S. Singh, and S. Puri, arXiv preprint arXiv:2509.05212 (2025).
- [63] J. Claes, arXiv preprint arXiv:2509.05232 (2025).
- [64] Y. Vaknin, [Github](#) (2025).
- [65] D. Bluvstein, S. J. Evered, A. A. Geim, S. H. Li, H. Zhou, T. Manovitz, S. Ebadi, M. Cain, M. Kalinowski, D. Hangleiter, *et al.*, *Nature* **626**, 58 (2024).
- [66] É. Gouzien and N. Sangouard, arXiv preprint arXiv:2503.15452 (2025).

APPENDIX

Appendix A: Noise model

We define the noise model similarly to uniform noise model as defined in [15], adding an additional term describing the noise coming from 3-qubit operation CCX . We introduce a 3-qubit depolarizing channel that applies one of the 63 (non-trivial) Pauli channels to the 3-qubits with equal probability $p/63$. The noise channels are defined in Fig. 9 and the uniform noise model, used throughout the paper, is defined in Fig. 10. This noise model is motivated by our decomposition of $CSWAP$ into CCZ , CX and single qubit rotations, see Fig. 13.

For Fig. 6, we used a simpler noise model, where single and two qubit depolarizing errors follow every single and two-qubit gate with the same probability p , with no idling or measurement errors.

Appendix B: Alternative Noise Model for Rydberg Atoms

Since our simulation assumes all-to-all connectivity, it would be most efficient to implement on a device with long range gates such as a Rydberg Atoms based quantum computer [24, 65]. Qubits based on Rydberg atoms can have coherence time much longer than their gate time. The dephasing error rate is dominated by decay during the excitation to the Rydberg state, which only happens during 2-Qubit gates. To label this effect, we changed the noise model of Fig. 10 by removing any idling error, and reducing the probability of single qubit errors to $p/10$. Since our scheme rarely uses 1-qubit gates to begin with, the dominant effect is removing the idling errors.

In Fig. 3, we can see improved logical fidelities, as high-weight errors are significantly less probable. As was demonstrated in [25, 26], there is a native implementation of a CCX gate Rydberg atom. It is therefore reasonable to expect future experiments would reduce the overhead of implementing CCX compared with the standard combination of multiple single and two qubit gates.

Appendix C: Full vector sampling

We used a full vector sampling in order to benchmark our protocol spending roughly 10^6 CPU hours resulting in roughly 10^7 shots for each point. We only benchmarked the H cultivation protocol using the unrotated surface code, and H_{XY} protocol using the rotated surface code. The results are shown in

Fig 11, in good agreement with the Clifford approximation, up to roughly a factor of 2.

We estimate the error bars in Fig 11 by considering variance of our Bernoulli variable, which is $\text{Var}(X) = (1 - p)p \approx p$. For N accepted shots with n_{error} errors, we set the error bars on our estimated p to be:

$$\sigma^2 = \frac{n_{\text{errors}}}{N^2}$$

Appendix D: Preparation and Measurement of the GHZ Ancilla state

The GHZ ancilla state is generated by first initializing all of its qubits in the $|0\rangle$ state beside a single *middle* qubit in the $|+\rangle$ state, and expanding the state in stages by repeated application of CX as seen in Fig. 1 and in [11].

As mentioned in the main text, the measurement is just the expansion step done in reverse. This is equivalent to the measurement in [11], but requires a few additional time steps. In [11], the stabilizers of the repetition code are measured in separate flag qubits, followed by measurement of all the qubits composing the GHZ state in X basis. Here, the application of the expansion step means that the stabilizer information can be measured by measuring the non-*middle* qubit in the Z basis. The logical measurement of the GHZ state can be recovered by measuring the *middle* qubit in the X basis.

Because of this equivalence, our GHZ measurement behaves as a one-flag circuit as defined in [11].

Appendix E: Cultivation with Erasure qubits and $d_1 = 2$

With erasure qubits, the residual Pauli error can reach low error rates. This suggests a simple proof of concept experiment for small devices with erasure qubits. Using a $d_1 = 2$ unrotated surface code that contains 5 data qubits and 4 ancilla, the logical H operator can be measured using a single 3-qubit gate (with the ancilla's doubling as GHZ ancilla). Because of the small distance of the code, only a single GHZ measurement is required. We simulated this protocol without erasure noise for various values of the Pauli noise using both of our noise models. The simulation includes the expansion to $d_2 = 11$. If we want to estimate how such experiment will behave with $e = 10^{-3}$ and $p = 10^{-4}$, the logical fidelity will approximately be the same as our simulation with $p = 10^{-4}$, and the rate can be deduced from the

Noise channel	Probability distribution of effects
MERR(p)	$1 - p \rightarrow$ (report previous measurement correctly) $p \rightarrow$ (report previous measurement incorrectly; flip its result)
XERR(p)	$1 - p \rightarrow I$ $p \rightarrow X$
ZERR(p)	$1 - p \rightarrow I$ $p \rightarrow Z$
DEP1(p)	$1 - p \rightarrow I$ $p/3 \rightarrow X$ $p/3 \rightarrow Y$ $p/3 \rightarrow Z$
DEP2(p)	$1 - p \rightarrow I$ $p/15 \rightarrow \{A \otimes B \mid A, B \in \{I, X, Y, Z\}, A \otimes B \neq I \otimes I\}$
DEP3(p)	$1 - p \rightarrow I$ $p/63 \rightarrow \{A \otimes B \otimes C \mid A, B, C \in \{I, X, Y, Z\}, A \otimes B \otimes C \neq I \otimes I \otimes I\}$

FIG. 9. **Definition of the various noise channels in the Clifford simulation** – The table was adapted from [15] with the addition of DEP3.

Ideal gate	Noisy gate
(single qubit unitary, including idle) U_1	$\text{DEP1}(p) \cdot U_1$
CX	$\text{DEP2}(p) \cdot CX$
CH_{XY}	$\text{DEP2}(p) \cdot CH_{XY}$
$C\bar{H}_{XY}$	$\text{DEP2}(p) \cdot C\bar{H}_{XY}$
CCX	$\text{DEP3}(3p) \cdot \text{DEP2}_{12}(p) \cdot \text{DEP2}_{13}(p) \cdot CCX$
$CSWAP \cdot CH^{\otimes 2}$	$\text{DEP3}(3p) \cdot \text{DEP2}_{12}(p) \cdot \text{DEP2}_{13}(p) \cdot CSWAP \circ CH^{\otimes 2}$
CCZ	$\text{DEP3}(3p) \cdot \text{DEP2}_{12}(p) \cdot \text{DEP2}_{13}(p) \cdot CCZ$
(reset) R_X	$ZERR(p) \cdot R_X$
R_Z	$XERR(p) \cdot R_Z$
M_X	$\text{DEP1}(p) \cdot \text{MERR}(p) \cdot M_X$
M_Z	$\text{DEP1}(p) \cdot \text{MERR}(p) \cdot M_Z$

FIG. 10. **Uniform noise model** Each perfect operation is replaced by a noisy version, with the noise channels defined in Fig. 9. The non-Clifford operations are replaced by CX 's which effectively measures the logical X or XX operators. The noise model doesn't change when replacing non-Clifford gates with Clifford gates. Subscripts in label the subset of qubits depolarized, with labeled as 1-Control, 2,3-Targets. Table adapted from [15] with some additions.

$p = 10^{-3}$ simulation, see Fig. 12. With these assumptions, we expect to reach 10^{-6} infidelity with rate exceeding 70% of shots. Without idling noise, we can further reach infidelities of 10^{-7} with over 85% acceptance rate.

Appendix F: CX cultivation with codes that encode multiple qubits

Since CX is transversal for all CSS codes, it can be used on pairs of codes that encode more than a single logical qubit. The eigenvalues of the transversal CX operator would still be ± 1 , but measuring it would not project every single logical qubit into the $|CX\rangle$ state. Instead, a $+1$ measurement would project the

qubits into an entangled state.

For a pair of $[[n, k, d]]$ quantum codes, the projection operator P_{\pm}^i projects two logical qubits, one from each code, to the ± 1 eigenspace of their combined logical CX operator. The index i labels the index of *both* qubits, each at their respective codes. If all of the stabilizers of both codes are initialized in the $+1$ eigenstate, then a $+1$ measurement of the transversal CX operator would effectively apply the following projection to the state:

$$\sum_{a \subseteq N} \prod_{i \notin a} P_+^i \prod_{j \in a} P_-^j, \quad (\text{F1})$$

where $N = \{a \mid a \subseteq \{1 \dots k\}, |a| \text{ is even}\}$, i.e. all sets of qubits with even size. This is different from pro-

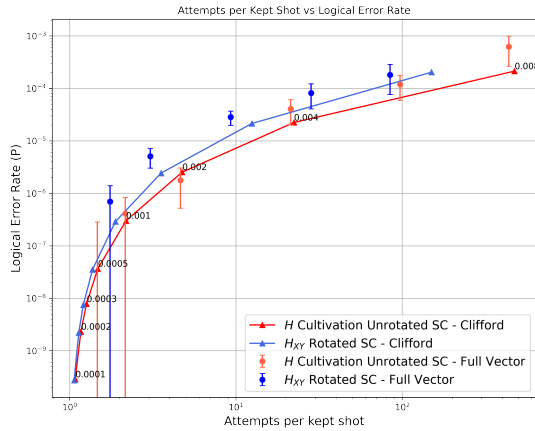


FIG. 11. Logical error rate of cultivation - comparing Clifford and Full Vector simulation – Logical error rate and acceptance rate of unrotated surface code H cultivation with Uniform noise model using both a full vector simulation (black) and an approximation using a Clifford simulator. The simulation doesn't include the expansion step and post selects on all stabilizer measurements before a final (perfect) logical measurement in the Magic state basis.

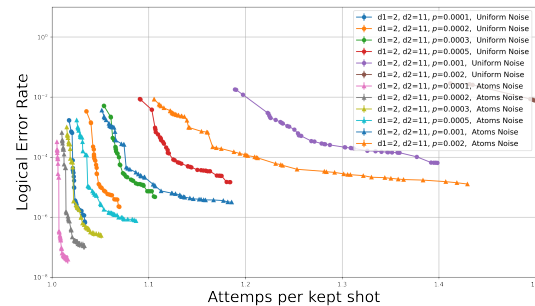


FIG. 12. **Logical error rate of H cultivation with expansion for $d_1 = 2$** – Logical error rate and acceptance rate of unrotated surface code H cultivation with Uniform and Atom noise model for $d_1 = 2$, following an expansion to $d_2 = 11$ unrotated surface code.

jecting all pairs of qubits into the $|\text{CX}\rangle$ state, which is achieved by the $\prod_{i < k} P_+^i$ operator.

More explicitly, define the state $|\overline{CX}\rangle = |1, -\rangle$ state, which is the single eigenstate with eigenvalue -1 of the CX operator. Projecting two $k = 2$ codes into the $+1$ eigenstate of the transversal CX operator would project the state into the following state:

$$|\text{CX}\rangle \otimes |\text{CX}\rangle + |\overline{\text{CX}}\rangle \otimes |\overline{\text{CX}}\rangle. \quad (\text{F2})$$

Since this state isn't composed of two copies of the

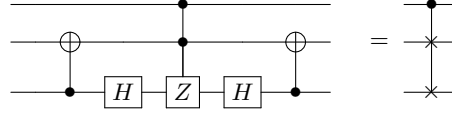


FIG. 13. Circuit Decomposition of 3-Qubit Controlled SWAP in terms of Clifford and CCZ gates.

Circuit decomposition of Controlled SWAP gate using native gates for cold atoms - a single CCZ and two *CX* gates. We verified that this decomposition is in fact optimal using the code provided in [66].

$|CX\rangle$ state, the method described in [8] can't directly translate it into the CCX state. It is possible that future schemes will allow it to be used to generate multiple useful magic states, that can effectively increase the rate of the cultivation procedure.

Appendix G: 3-Qubit gate compilation

Our cultivation schemes make use of three types of three-qubit gates. As noted above, certain trapped-atom platforms natively support *CCZ* gates, which simplify the implementation of *CCX*. For the *CSWAP* gate, we employed the compilation from [66] (see Fig. 13), yielding an optimal decomposition that requires only two additional *CX* gates.

In our noise model, each three-qubit gate is followed by a $\text{DEPOLARIZE3}(3p)$ channel with probability $3p$, where p denotes the two-qubit gate error rate for the rest of the circuit. Since three-qubit gates are used sparingly in the protocol, the overall performance is not highly sensitive to this assumption. Figure G shows the effect of varying the noise strength of the $\text{DEPOLARIZE3}(p_{3Q})$ term while fixing $p = 10^{-3}$. Even when p_{3Q} is increased by more than an order of magnitude, the logical error rate and fidelity are affected by less than a factor of two.

Appendix H: Initialization and injection

Here, we provide here additional details on the initialization steps of our cultivation protocols. Each protocol begins by resetting all data qubits to either the $|0\rangle$ or $|+\rangle$ state. Specifically, for H cultivation we initialize in $|0\rangle$; for H_{XY} we initialize in $|+\rangle$; and for CX cultivation we set the control patch to $|+\rangle$ and the target patch to $|0\rangle$.

As is standard for CSS codes, this initialization fixes half of the stabilizers to the $+1$ eigenstate—namely, those aligned with the basis of the

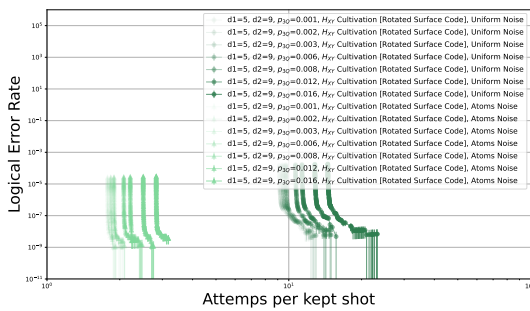


FIG. 14. Logical fidelity and acceptance rate as a function of p_{3Q} .

Logical error rate and acceptance rate of rotated surface code H_{XY} cultivation with Uniform and Atom noise model, with varying strength for p_{3Q} and constant $p = 10^{-3}$. In the main text, all of our simulations used $p_{3Q} = 3p = 3 \times 10^{-3}$, as described in A.

initialized data qubits. The remaining stabilizers are left in random eigenstates. To enforce that all stabilizers are in the $+1$ eigenstate, we perform a syndrome extraction step to identify the randomly assigned stabilizers and then apply conditional single-qubit gates to flip any -1 outcomes to $+1$.

Following these corrections, we proceed with state injection. For H_{XY} cultivation, we collapse the weight-3 logical Z operator onto a single qubit using a pair of CX gates. We then rotate that qubit by $\pi/8$ around the Z axis and apply the CX gates in reverse, preparing the surface-code patch in the $|T\rangle$ state.

For H cultivation, we instead perform two successive rotations: a $\pi/8$ rotation about the logical X axis, followed by a $\pi/4$ rotation about the logical Z axis. These operations initialize the surface-code patch in the $|T_H\rangle$ state.

We then perform an additional syndrome extraction round, and post select on any faulty syndrome.

Appendix I: Full protocol as pseudo-code

Below we provide pseudocode for the H cultivation protocol on the unrotated surface code.

In the rotated surface code, each double-check is performed by inserting it between the two halves of a syndrome extraction CX cycle. We follow this by post-selecting on the absence of any -1 syndrome outcomes.

Algorithm 1 Pseudocode for Cultivation on an Unrotated Surface Code

Require: Projection operator $P \in \{H, H_{XY}\}$, code distance parameter $d_1 \in \{3, 5\}$, complementary gap threshold τ , final distance d_2

- 1: Initialize a $d = 3$ unrotated surface code
- 2: **if** $P = H$ **then**
- 3: Initialize data qubits in $|0\rangle$
- 4: **else if** $P = H_{XY}$ **then**
- 5: Initialize data qubits in $|+\rangle$
- 6: **end if**
- 7: Run a single round of syndrome extraction
- 8: Post-select on Z stabilizers (for H) or X stabilizers (for H_{XY}) in the -1 state
- 9: **if** $P = H$ **then**
- 10: Apply Z corrections to set all X stabilizers to $+1$
- 11: Rotate around the logical X axis by $\pi/8$
- 12: Rotate around the logical Z axis by $\pi/4$
- 13: **else if** $P = H_{XY}$ **then**
- 14: Apply X corrections to set all Z stabilizers to $+1$
- 15: Rotate around the logical Z axis by $\pi/8$
- 16: **end if**
- 17: Run a single round of syndrome extraction
- 18: Post-select on any stabilizers in the -1 state
- 19: *Double-check* the logical operator
- 20: **if** $d_1 = 5$ **then**
- 21: Expand the code to $d = 5$ with all stabilizers in the $+1$ eigenstate using a unitary circuit
- 22: Run a single round of syndrome extraction
- 23: Post-select on any stabilizers in the -1 state
- 24: *Double-check* the logical operator
- 25: **end if**
- 26: Expand the code to d_2
- 27: Run 10 rounds of syndrome extraction
- 28: Decode and post-select using the complementary gap threshold τ
